# Communication

## Wideband Decoupling of Integrated Slot Antenna Pairs for 5G Smartphones

Libin Sun, Yue Li, and Zhijun Zhang

***Abstract*— This communication proposes a wideband decoupling technique to suppress the strong coupling between two extremely closely spaced open-slot antennas and implements a wideband integrated slot antenna pair for fifth-generation (5G) metal-rimmed smartphones. By simply inserting a connecting line between two closely spaced open-slot antennas, a top slot structure can be constituted with odd- and even-mode resonances in the lower and higher bands, respectively, to cancel the original strong mutual coupling. In addition to the decoupling effect, the top slot can also expand the effective radiation aperture of the antenna pair for the bandwidth improvement. The proposed slot antenna pair, with a compact footprint of 28 × 7 × 1.8 mm$^3$, shows good impedance matching, isolated and diversity performance across 3.3–5.0 GHz. Then, an 8 × 8 multiple-input multiple-output (MIMO) system, constituted by four sets of slot antenna pairs, is simulated, fabricated, and measured. Both the simulated and experimental results show that the 8 × 8 MIMO system can offer isolations of better than 10.8 dB and envelope correlation coefficients (ECCs) of less than 0.14 between all eight ports across 3.3–5.0 GHz. Also, a total efficiency of 55.0%–83.1% and 52.5%–83.1% is achieved for Ant1 and Ant2, respectively. Featuring wide bandwidth, compact size, high integration level, and metal rim compatibility, we forecast the proposed solution has great potential for future 5G smartphones.**

***Index Terms*— Antenna decoupling, antenna pair, fifth-generation (5G), multiple-input multiple-output (MIMO), smartphone antennas.**

### I. Introduction

Recently, fifth-generation (5G) technology is rapidly developed to provide higher throughput and shorter latency in wireless communication systems [1]. As one of key techniques of 5G systems, multiple-input multiple-output (MIMO) can linearly enhance the channel capacity without exploiting extra spectrum or power resources. In 5G smartphones, four to eight MIMO antennas operating at sub-6 GHz spectrum are implemented to transfer multiple data streams simultaneously for single users. However, owing to the limited space allocation and complex environment in up-to-date smartphones, the design of 5G MIMO antennas faces three major challenges. First, effective decoupling techniques should be utilized to reduce the spatial distance between multiple antennas for fitting the size-limited environment. Second, antennas should be codesigned with the metal rim, which is widely applied in mainstream smartphones. Third, wide bandwidth should be realized to satisfy the global 5G spectrums: N77 (3.3–4.2 GHz), N78 (3.3–3.8 GHz), and N79 (4.4–5.0 GHz) [2].

To solve the contradiction between spatial distance and antenna isolation, different decoupling techniques are proposed for closely spaced or shared-radiator antenna elements [3]–[20]. In [3] and [4], neutralization line technique is employed to mitigate the mutual coupling between closely spaced slot or monopole antennas. In [5]–[8], lumped inductance or capacitance is used to build an *LC* tank between closely spaced inverted-F antennas (IFAs) for the coupling suppression. Alternatively, the lumped components could be replaced by distributed structures [9]–[11]. Wong *et al.* [12] and [13] proposed a novel gap-coupled loop antenna pair with self-decoupling performance even in the closely spaced configuration. In [14]–[19], an orthogonal mode method is proposed to realize a natural high isolation between two closely spaced or shared-radiator antenna elements without exploiting any extra decoupling structures. In [20], a novel self-decoupled dual-fed strip antenna pair is proposed.

Compared with the traditional design scheme with eight separated antenna elements [21]–[35], the integrated yet decoupled dual-antenna building blocks [3]–[20] show improved space utilization for fitting the size-limited environment in 5G smartphones. However, the narrow bandwidth of the above building blocks [3]–[10], [12]–[18], [20] makes them unsuitable for future global 5G smartphones. In addition, the metal rim incompatibility property [3]–[16], [20] also makes them incompetent for mainstream smartphones. Therefore, designing wideband and integrated antenna pair with metal rim compatibility is one of the development trends of 5G smartphone antennas.

In this communication, a dual-mode decoupling technique is proposed to suppress the strong coupling between two closely spaced open-slot antennas across a wide bandwidth by simply inserting a connecting line in between. Individual mode analysis of common mode (CM) and differential mode (DM) is performed to better understand the formation of the proposed two decoupling modes in the lower and higher frequency, respectively. The simulated results demonstrate that the integrated slot antenna pair shows a wide operating bandwidth of 3.3–5.0 GHz with both $S_{11} < -6$ dB and $S_{21} < -10$ dB. Also, a high total efficiency of 62.0%–81.0% and a good diversity performance of envelope correlation coefficient (ECC) less than 0.15 are achieved. Furthermore, an 8 × 8 MIMO antenna system, constituted by four sets of integrated slot antenna pairs, is simulated, fabricated, and measured to validate the feasibility of the proposed design scheme.

### II. Evolution Process

#### A. Case 1: Decoupling Between Two IFAs by an Inductor

The IFA is widely exploited in mobile phone antennas due to its low profile. Fig. 1(a) shows two closely spaced IFAs separated by 1 mm ($0.0125\lambda_L$). The original isolation between two elements is only 4.9 dB without decoupling. Then, by simply inserting a lumped inductance in between [5], the coupling *E*-fields can be blocked because the lumped inductance and the coupling capacitance can form a parallel *LC* tank with a band-stop response. As shown in Fig. 1(d), the isolation is improved to better than 11.3 dB across the matched bandwidth of 3.75–4.35 GHz (14.8%).

#### B. Case 2: Decoupling Between Slot Antennas by an Inductor

Although good decoupling performance is realized by the inserted inductance [5], the bandwidth is still limited. To further enhance the

Manuscript received January 15, 2020; revised August 4, 2020; accepted August 22, 2020. Date of publication September 11, 2020; date of current version April 7, 2021. This work was supported in part by the National Natural Science Foundation of China under Contract 61971254 and Contract 61525104, and in part by the National Key Research and Development Program of China under Grant 2018YFB1801603. *(Corresponding author: Zhijun Zhang.)*

The authors are with the Beijing National Research Center for Information Science and Technology (BNRist), Tsinghua University, Beijing 100084, China (e-mail: zjzh@tsinghua.edu.cn).

Color versions of one or more of the figures in this communication are available online at https://ieeexplore.ieee.org.

Digital Object Identifier 10.1109/TAP.2020.3021785

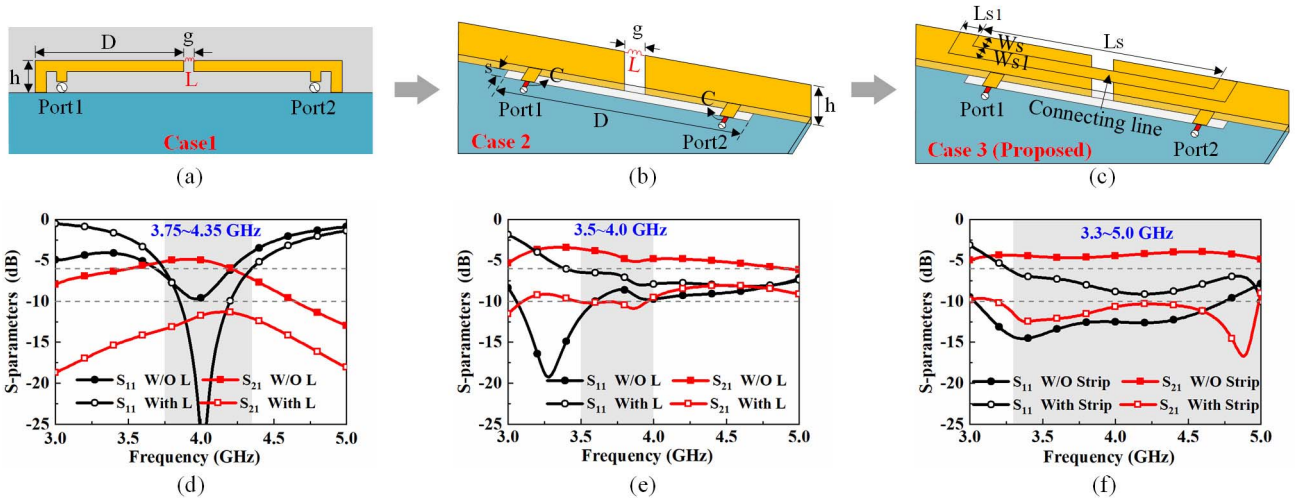


Fig. 1. Evolution procedure of the wideband integrated slot antenna pair. (a) Case 1: decoupling between two IFAs by an inserted inductor [5]: $D = 14$ mm, $h = 3$ mm, $g = 1$ mm, $L = 21$ nH. (b) Case 2: decoupling between two open-slot antennas by an inserted inductor: $D = 28$ mm, $h = 6$ mm, $s = 2$ mm, $g = 3$ mm, $C = 0.6$ pF, $L = 16$ nH. (c) Case 3: decoupling between two open-slot antennas by a connecting line: $D = 28$ mm, $h = 6$ mm, $s = 2$ mm, $g = 3$ mm, $C = 0.75$ pF, $L_s = 26$ mm, $L_{s1} = 2$ mm, $W_s = 2$ mm, $W_{s1} = 2$ mm. (d)–(f) Simulated $S$-parameters of Cases 1–3.

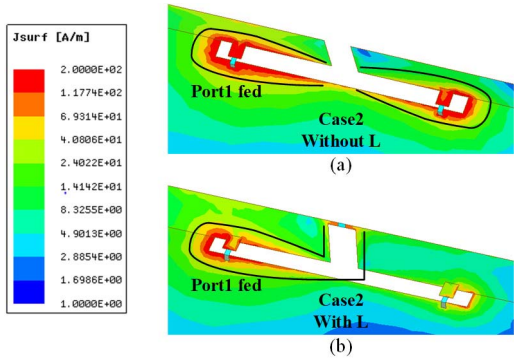


Fig. 2. Simulated current distributions of Case 2 at 3.75 GHz (a) without and (b) with the decoupling inductance.

bandwidth and accommodate to the metal rim, the IFA is codesigned with the metal rim of the smartphone, as shown in Fig. 1(b). Owing to the thick periphery of the metal rim, the open-slot mode, instead of the IFA mode, is dominantly radiated with an enhanced $-6$ dB $S_{11}$ bandwidth as shown in Fig. 1(e). The inserted lumped inductance can also suppress the strong coupling between closely spaced open-slot antennas. Fig. 2(a) and (b) shows the current distributions without and with the decoupling inductance, respectively. As shown in Fig. 2(a), a balanced slot mode is excited when fed through Port 1 with a strong coupling between two symmetrical ports. With the help of the inserted lumped inductance, as shown in Fig. 2(b), the strong coupling can be suppressed with an unbalanced open-slot mode excited. However, the inductance decoupling technique cannot realize a wide decoupling bandwidth. As shown in Fig. 1(e), the optimized $-10$ dB $S_{21}$ bandwidth is only from 3.5 to 4.0 GHz (13.3%).

### C. Case 3: Wideband Decoupling by a Connecting Line

As shown in Fig. 1(c), if we substitute the lumped inductance by a metal connecting line between two closely spaced open-slot antennas to construct an integrated slot antenna pair, the impedance matching and decoupling bandwidth can be significantly enhanced to 3.3–5.0 GHz (41.0%) as shown in Fig. 1(f), which can satisfy the bandwidth requirement of global 5G N77, N78, and N79 spectrums. The inserted connecting line, combined with the metal rim of the smartphone, can constitute a top slot structure, which can offer two different modes to cancel the original mutual coupling in the lower and higher bands, respectively. In addition to the decoupling effect, the top slot can also be a radiator to expand the effective radiation aperture for the bandwidth enhancement. To clearly interpret the decoupling mechanism of the connecting line, the mode analysis will be performed in Section III based on the mode cancellation method [20].

## III. Decoupling Mechanism and Simulated Results

### A. Decoupling Mechanism

For a symmetric and reciprocal two-port antenna system, it is theoretically demonstrated that the mutual coupling effect between two antennas can be totally eliminated when CM and DM impedances are the same according to the equation [20]

$$S_{21} = (S_{cc11} - S_{dd11})/2 \tag{1}$$

where $S_{cc11}$ and $S_{dd11}$ are the CM and DM reflection coefficients, respectively. Due to the orthogonal nature of CM and DM, the CM and DM could be regarded as a set of orthogonal basis of the two-port system. Accordingly, the operating mode that fed through Port 1 can be equivalent to the addition of CM and DM

$$\boldsymbol{E}_{P1} = \boldsymbol{E}_{\mathrm{CM}} + \boldsymbol{E}_{\mathrm{DM}}. \tag{2}$$

And the operating mode that fed through Port 2 can be equivalent to the subtraction of CM and DM

$$\boldsymbol{E}_{P2} = \boldsymbol{E}_{\mathrm{CM}} - \boldsymbol{E}_{\mathrm{DM}}. \tag{3}$$

Fig. 3(a) and (b) plots the CM $E$-field distributions at the lower (3.4 GHz) and higher (4.9 GHz) frequency, respectively. As seen, in the lower frequency, the bottom slot is excited with a balanced slot mode, whereas the $E$-field in the top slot is very weak. In the higher band, however, the top slot is excited due to the strong electrical coupling between bottom and top slots.

Fig. 3(c) and (d) plots the DM $E$-field distributions at 3.4 and 4.9 GHz, respectively. As seen, in the lower band, both the bottom

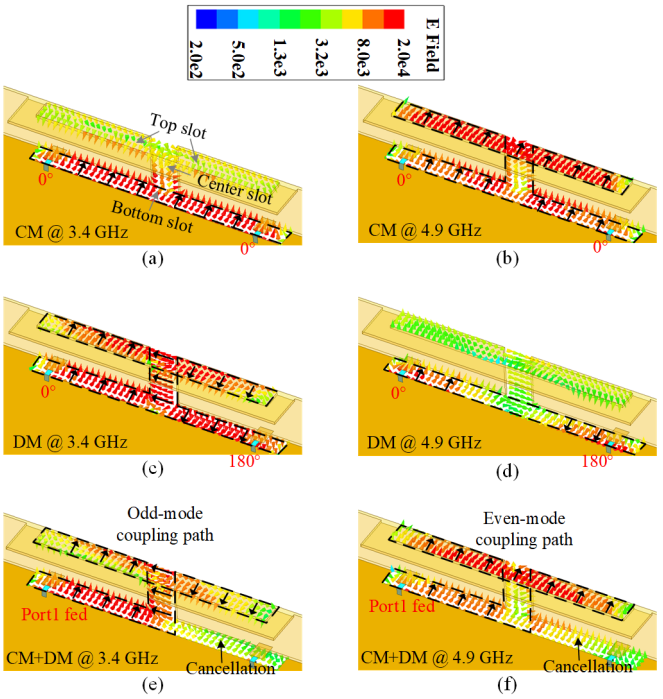


Fig. 3. E-filed distributions under different feeding cases to demonstrate the decoupling mechanism. (a) CM at 3.4 GHz. (b) CM at 4.9 GHz. (c) DM at 3.4 GHz. (d) DM at 4.9 GHz. (e) Port 1 fed at 3.4 GHz. (f) Port 1 fed at 4.9 GHz.

and top slots are excited simultaneously with antiphase slot modes. Compared with CM, the DM operates at lower frequency due to the ground current radiation of the unbalanced mode [16]. In the higher band, however, the top slot is not effectively excited with only a localized resonance in the bottom slot.

Fig. 3(e) and (f) plots the $E$-field distributions at 3.4 and 4.9 GHz when fed through Port 1, which can be regarded as the superposition of CM and DM $E$-fields in terms of (2). In the lower frequency, as shown in Fig. 3(e), the $E$-field distribution in the right half of the bottom slot is canceled due to the out-of-phase cancellation of CM and DM $E$-fields thereof. And in the top slot is an antiphase slot mode due to the dominant resonant effect of DM in the lower band. Therefore, in the lower band, the top slot is an odd-mode resonator, and it can offer an odd-mode coupling path to cancel the original strong mutual coupling. In the higher band, as shown in Fig. 3(f), the $E$-field distribution in the right half of the bottom slot is also canceled due to the out-of-phase cancelation of CM and DM $E$-fields thereof. On the contrary, in the top slot is an in-phase slot mode due to the dominant resonant effect of CM in the higher band. Therefore, in the higher band, the top slot is an even-mode resonator, and it can offer an even-mode coupling path to cancel the original strong mutual coupling. With the combination of the odd- and even-mode resonators in the lower and higher bands, dual-band or wideband decoupling performance can be realized. Note that the proposed decoupling mechanism is different from the conventional neutralization line technique [36].

1) Extra slot coupling modes instead of the line coupling mode are utilized to cancel the original mutual coupling.
2) Dual-mode decoupling is realized by the combination of the odd and even coupling modes.
3) The top slot is not only a decoupling structure, but also a radiator to further expand the radiation aperture and increase the bandwidth of the antenna pair.

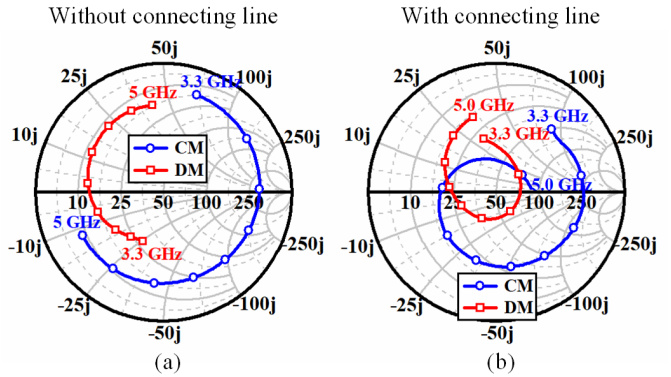


Fig. 4. Smith charts of CM and DM reflection coefficients (a) without and (b) with the connecting line.

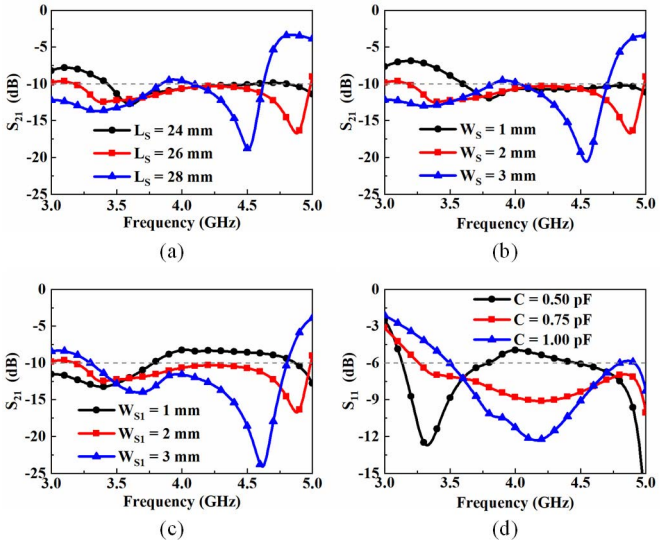


Fig. 5. Parameter analysis. (a) $S_{21}$ versus $L_s$. (b) $S_{21}$ versus $W_s$. (c) $S_{21}$ versus $W_s1$. (d) $S_{11}$ versus capacitance $C$.

The Smith charts of CM and DM reflection coefficients without and with the connecting line are also presented to analyze the effect of the connecting line from the perspective of CM and DM impedances. Without the connecting line, as shown in Fig. 4(a), the CM impedance is far away from the DM impedance, leading to a poor isolation between two ports according to (1). After connecting a line in between, as shown in Fig. 4(b), the CM impedance matching in the higher band is improved with the help of the new resonant mode in the top slot, as shown in Fig. 3(b), which indicates the top slot is also a radiator to improve the bandwidth. Meanwhile, the DM impedance matching in the lower band is also improved with the help of the new resonant mode in the top slot, as shown in Fig. 3(c). With improved impedance matching for both CM and DM, the CM and DM impedances are much close to each other, contributing to an enhanced isolation between two closely spaced open-slot antennas.

### *B. Parameter Analysis*

Some key parameters are studied in Fig. 5 to demonstrate the design and optimized process of the proposed integrated slot antenna pair. The length and width of the top slot, that is, $L_s$ and $W_s$, are two vital parameters to tune the frequency of $S_{21}$. Both the lower and higher bands can be adjusted simultaneously because the top slot is excited in both bands. As shown in Fig. 5(a) and (b), with the increase of $L_s$ and $W_s$, both of the lower and higher frequency shift downward.

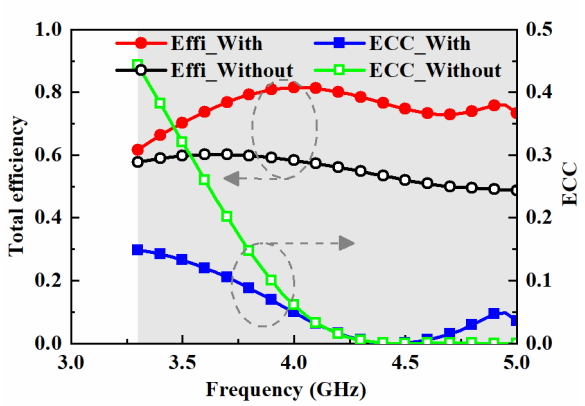


Fig. 6. Simulated total efficiency and ECC of the integrated slot antenna pair with and without the connecting line.

The width of connecting line, that is, $W_{s1}$, has different effect on the lower and higher decoupling frequency. As shown in Fig. 5(c), with the increasing of $W_{s1}$, the resonant frequency of the antiphase slot mode (lower band) will be increased and that of the in-phase slot mode (higher band) will be decreased. Therefore, $W_{s1}$ is an important means to adjust the operating bandwidth.

At each port, a lumped capacitance is added to tune the impedance matching of the antenna element. As shown in Fig. 5(d), with an appropriate capacitance value of $C = 0.75$ pF, a good impedance matching of $S_{11} < -6$ dB across the entire band of 3.3–5.0 GHz can be achieved.

### C. Radiation and Diversity Performance

To evaluate the diversity performance of the proposed integrated slot antenna pair, the ECC with and without the connecting line is calculated by the simulated radiated far field [37]. As shown in Fig. 6, the ECC is optimized from 0.44 to 0.15 in the lower band with the help of the connecting line, and a good diversity performance of ECC $< 0.15$ across 3.3–5.0 GHz is realized. The simulated total efficiency with and without the connecting line is also presented in Fig. 6. Owing to the symmetrical structure, the antenna efficiency of Ant1 is same with Ant2. As seen, an average efficiency enhancement of 20.0% is achieved with the help of the decoupling structure, and a high total efficiency of 62.0%–81.0% is fulfilled across 3.3–5.0 GHz.

## IV. 8 × 8 MIMO System

### A. Antenna Structure

By placing four sets of the proposed integrated slot antenna pair along two side edges of the smartphone, an 8 × 8 MIMO antenna system is realized as shown in Fig. 7. The ground plane (in blue) is printed on the bottom side of the FR-4 ($\varepsilon_r = 4.4$, $\tan\delta = 0.02$) substrate (145 × 75 × 0.8 mm$^3$), while eight 50 Ω feed lines (in red) are printed on the top side of the FR-4 substrate. For every antenna element, a 0.75 pF lumped capacitance is soldered in the feedline for impedance matching. A full circle of metal rim, with a thickness of 0.3 mm, is vertically surrounded the FR-4 substrate and connected with the ground plane. For each antenna pair, only one rim slot is required due to the rim slot reuse, which is superior to the up-to-date wideband 5G metal-rimmed smartphone antenna with eight rim slots for the 8 × 8 MIMO system [19], [32], [33]. The detailed dimension is reoptimized by HFSS and listed in Table I. The footprint of the integrated slot antenna pair is $D \times H \times s = 28 \times 7 \times 1.8$ mm$^3$.

To validate the feasibility of the proposed 8 × 8 MIMO system, a prototype was fabricated as shown in Fig. 8. The main board of smartphone is manufactured by a 0.8 mm thick FR-4 substrate with

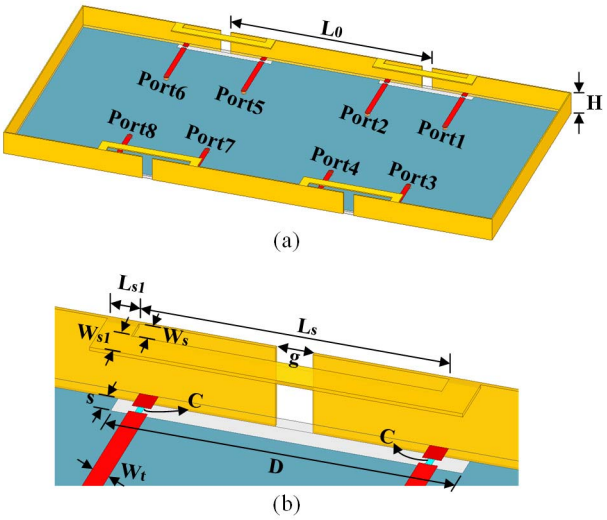


Fig. 7. (a) Geometry of the 8 × 8 MIMO antenna system. (b) Geometry of the integrated slot antenna pair.

TABLE I
DETAILED DIMENSIONS (UNIT: mm)

| Parameter | $L_0$ | $L_s$ | $L_{s1}$ | $W_s$ | $W_{s1}$ |
|---|---|---|---|---|---|
| Value | 60 | 25 | 2.5 | 1.8 | 2.7 |
| Parameter | g | s | D | H | $W_t$ |
| Value | 3 | 1.8 | 28 | 7 | 1.5 |

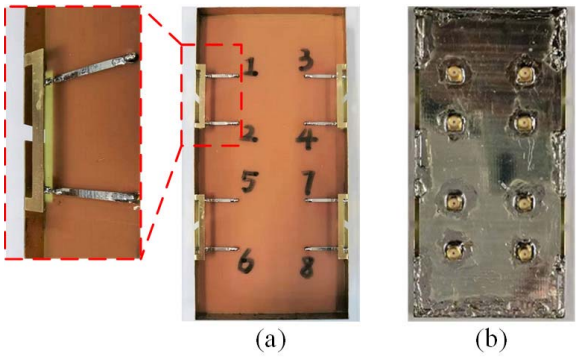


Fig. 8. Photograph of the fabricated 8 × 8 MIMO system. (a) Top view: inset is the enlarged view of the integrated slot antenna pair. (b) Bottom view.

the ground plane and feed lines printed on the bottom and top sides, respectively. The metal rim, combined with the connecting lines, is manufactured by 0.3 mm thick brass sheets with laser cutting process. The metal rim is soldered with the ground plane of the main board for the common ground. Eight 50 Ω SMA connectors are soldered with the feedlines for antenna test.

### B. Simulated and Measured Results

The simulated and measured $S$-parameters of the integrated slot antenna pair in the 8 × 8 MIMO system are presented in Fig. 9. As seen, the measured result shows a good agreement with the simulated result. The measured reflection coefficients are less than −7.3 dB across 3.3–5.0 GHz for both Ant1 and Ant2. Also, the measured isolation between Ant1 and Ant2 is better than 10.8 dB across 3.3–5.0 GHz.

TABLE II
COMPARISONS OF THE UP-TO-DATE 5G MIMO TERMINAL ANTENNAS

| Ref. | Decoupling Method | Integrated Ant. Pair | Metal Rim | Bandwidth | Size of Ant. Pair (Length ×Height × Ground clearance) | Isolation of Ant. Pair | Total Efficiency |
|---|---|---|---|---|---|---|---|
| [5] | Lumped inductance | √ | × | 3.4-3.8 GHz | [a]20×4 mm$^2$ | >16.5 dB | 50~74% |
| [6] | Lumped capacitance | √ | × | 3.3-4.0 GHz | [b]20×6 mm$^2$ | >12 dB | 52~74% |
| [10] | Grounded strip | √ | × | 3.4-3.6 GHz<br>4.8-5.0 GHz | 22×7×1.8 mm$^3$ | >17.5 dB<br>>20 dB | >50% |
| [11] | Grounded strip | √ | × | 3.3-5.0 GHz<br>5.15-5.875 GHz | 35×7×1 mm$^3$ | >12 dB | 56~83% |
| [12] | Asymmetrically mirrored | √ | × | 3.4-3.6 GHz | 10×7×1 mm$^3$ | >10 dB | 40-52% |
| [15] | Orthogonal mode | √ | × | 3.4-3.6 GHz | 12×7×1.8 mm$^3$ | >20 dB | 49-72.9% |
| [16] | Orthogonal mode | √ | × | 3.4-3.61 GHz | 15×7×0.8 mm$^3$ | >24 dB | 41.2-60.4%<br>41.0-55.4% |
| [17] | Orthogonal mode | √ | √ | 3.4-3.6 GHz | 25×7×1.5 mm$^3$ | >20.1 dB | 35.2-64.7% |
| [19] | Orthogonal mode | √ | √ | 3.3-5.0 GHz | 40×7.5×3 mm$^3$ | >21 dB | 58.9-88.6%<br>31.6-76.7% |
| [20] | Self-decoupled | √ | × | 3.3-4.2 GHz | 30×7.5×2 mm$^3$ | >10.5 dB | 63.1-85.1% |
| [32] | Spatial diversity | × | √ | 3.3-6.0 GHz | \ | \ | 40.0-71.0% |
| [33] | Spatial diversity | × | √ | 3.3-7.1 GHz | \ | \ | 47.0-71.0% |
| **Proposed** | **Connecting line** | √ | √ | **3.3-5.0 GHz** | **28×7×1.8 mm$^3$** | **>10.8 dB** | **55.0-83.1%<br>52.5-83.1%** |

[a] The antenna pair is a planar structure with a length of 20 mm and a ground clearance of 4 mm.
[b] The antenna pair is a planar structure with a length of 20 mm and a ground clearance of 6 mm.

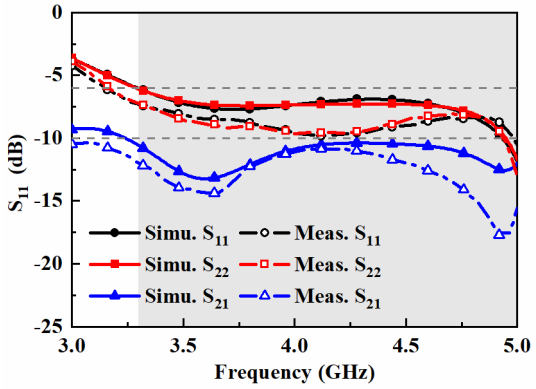


Fig. 9. Simulated and measured *S*-parameters of the integrated slot antenna pair in the 8 × 8 MIMO system.

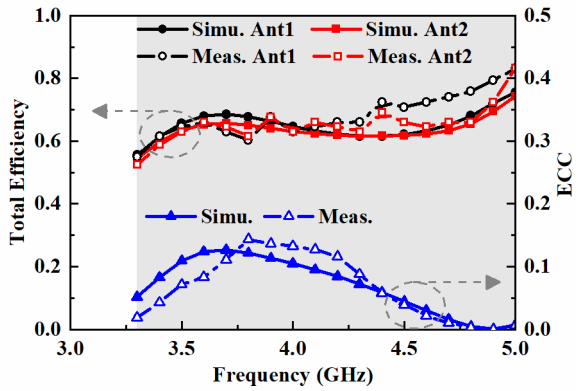


Fig. 10. Simulated and measured total efficiency and ECC of the integrated slot antenna pair in the 8 × 8 MIMO system.

To evaluate the radiation and diversity performance of the integrated slot antenna pair in the 8 × 8 MIMO system, the simulated and measured total antenna efficiencies and ECCs are proposed in Fig. 10. Note that the simulated and measured ECCs are calculated by the simulated and measured far fields [37], respectively. As seen, the simulated ECC is less than 0.13 whereas the measured result is less than 0.14, indicating a good diversity performance between two integrated slot antennas. Also, the simulated antenna efficiencies are 55.5%–75.0% and 54.5%–74.2% for Ant1 and Ant2, respectively, while the measured results are 55.0%–83.1% and 52.5%–83.1% for Ant1 and Ant2, respectively. There is a small discrepancy between simulated and measured results due to the manual fabrication error.

With the help of the spatial diversity, the isolations and ECCs between every antenna pair are better than 15.0 dB and less than 0.06, respectively, which is not shown for brevity.

### C. Comparison

The advantages of the proposed integrated slot antenna pair are highlighted by comparing with the up-to-date 5G MIMO terminal antennas as shown in Table II. As seen, most of the up-to-date 5G MIMO antenna pairs can only cover a narrow bandwidth and incompatible with the metal rim of the smartphone. In [11], a wide-band antenna pair is proposed with both 5G N77/N78/N79 and WLAN (5150–5875 MHz) bands covered; however, this work is unsuitable for the metal-rimmed smartphones. In [19], a novel orthogonal-mode antenna pair is presented with both wideband and metal rim compatible performance. However, the overall size of [19] is too large for the size-limited environment in smartphones. Compared with [19], the proposed work has a significant volume reduction

from 900 to 352.8 mm$^3$ with both the antenna length and ground clearance compressed. Therefore, the proposed work paves the way for the size reduction of wideband-integrated antenna pair, which is a promising candidate for the future 5G metal-rimmed smartphones.

## V. Conclusion

This communication proposes a dual-mode decoupling technique for closely spaced open-slot antennas to form a wideband integrated slot antenna pair. By inserting a connecting line between two closely spaced open-slot antennas, a wide decoupling bandwidth of 3.3–5.0 GHz is fulfilled with the combination of the odd decoupling mode in the lower band and the even decoupling mode in the higher band. The integrated slot antenna pair, with a footprint of $28 \times 7 \times 1.8$ mm$^3$, shows $S_{11} < -6$ dB, $S_{21} < -10$ dB, ECC $< 0.15$, and total efficiency large than 62.0% across 3.3–5.0 GHz. Moreover, an $8 \times 8$ MIMO antenna system, constituted by four sets of slot antenna pairs, is proposed to validate the idea. Both the simulated and measured results demonstrate that the $8 \times 8$ MIMO antenna system can offer good isolations of better than 10.8 dB and ECCs of less than 0.14 between all eight ports across the 5G N77, N78, and N79 bands. The proposed integrated slot antenna pair, with advantages of high integration level, wide bandwidth, compact size, and metal rim compatibility over the existing design scheme, has the potential for the application of future 5G smartphones.

## References


[1] J. G. Andrews *et al.*, "What will 5G be?" *IEEE J. Sel. Areas Commun.*, vol. 32, no. 6, pp. 1065–1082, Jun. 2014.

[2] *5G NR (New Radio)*. Accessed: May 28, 2019. [Online]. Available: http://3gpp.org/

[3] K.-L. Wong, J.-Y. Lu, L.-Y. Chen, W.-Y. Li, and Y.-L. Ban, "8-antenna and 16-antenna arrays using the quad-antenna linear array as a building block for the 3.5-GHz LTE MIMO operation in the smartphone," *Microw. Opt. Technol. Lett.*, vol. 58, no. 1, pp. 174–181, Jan. 2016.

[4] X. Shi, M. Zhang, S. Xu, D. Liu, H. Wen, and J. Wang, "Dual-band 8-element MIMO antenna with short neutral line for 5G mobile handset," in *Proc. 11th Eur. Conf. Antennas Propag. (EUCAP)*, Mar. 2017, pp. 3140–3142.

[5] K.-L. Wong and L.-Y. Chen, "Dual-inverted-F antenna with a decoupling chip inductor for the 3.6-GHz LTE operation in the tablet computer," *Microw. Opt. Technol. Lett.*, vol. 57, no. 9, pp. 2189–2194, Sep. 2015.

[6] K. Wong, B. Lin, and S. Lin, "High-isolation conjoined loop multi-input multi-output antennas for the fifth-generation tablet device," *Microw. Opt. Technol. Lett.*, vol. 61, no. 1, pp. 111–119, Jan. 2019.

[7] J. Sui and K.-L. Wu, "Self-curing decoupling technique for two inverted-F antennas with capacitive loads," *IEEE Trans. Antennas Propag.*, vol. 66, no. 3, pp. 1093–1101, Mar. 2018.

[8] C. Deng, D. Liu, and X. Lv, "Tightly arranged four-element MIMO antennas for 5G mobile terminals," *IEEE Trans. Antennas Propag.*, vol. 67, no. 10, pp. 6353–6361, Oct. 2019.

[9] Z. Ren, A. Zhao, and S. Wu, "MIMO antenna with compact decoupled antenna pairs for 5G mobile terminals," *IEEE Antennas Wireless Propag. Lett.*, vol. 18, no. 7, pp. 1367–1371, Jul. 2019.

[10] Z. Ren and A. Zhao, "Dual-band MIMO antenna with compact self-decoupled antenna pairs for 5G mobile applications," *IEEE Access*, vol. 7, pp. 82288–82296, 2019.

[11] K. L. Wong, Y. H. Chen, and W. Y. Li, "Decoupled compact ultra-wideband MIMO antennas covering 3300 6000 MHz for the fifth-generation mobile and 5GHz-WLAN operations in the future smartphone," *Microw. Opt. Technol. Lett.*, vol. 60, no. 10, pp. 2345–2351, Oct. 2018.

[12] K.-L. Wong, C.-Y. Tsai, and J.-Y. Lu, "Two asymmetrically mirrored gap-coupled loop antennas as a compact building block for eight-antenna MIMO array in the future smartphone," *IEEE Trans. Antennas Propag.*, vol. 65, no. 4, pp. 1765–1778, Apr. 2017.

[13] K.-L. Wong, B.-W. Lin, and B. W.-Y. Li, "Dual-band dual inverted-F/loop antennas as a compact decoupled building block for forming eight 3.5/5.8-GHz MIMO antennas in the future smartphone," *Microw. Opt. Technol. Lett.*, vol. 59, no. 11, pp. 2715–2721, Nov. 2017.

[14] L. Sun, H. Feng, Y. Li, and Z. Zhang, "Tightly arranged orthogonal mode antenna for 5G MIMO mobile terminal," *Microw. Opt. Technol. Lett.*, vol. 60, no. 7, pp. 1751–1756, Jul. 2018.

[15] L. Sun, H. Feng, Y. Li, and Z. Zhang, "Compact 5G MIMO mobile phone antennas with tightly arranged orthogonal-mode pairs," *IEEE Trans. Antennas Propag.*, vol. 66, no. 11, pp. 6364–6369, Nov. 2018.

[16] L. Chang, Y. Yu, K. Wei, and H. Wang, "Orthogonally polarized dual antenna pair with high isolation and balanced high performance for 5G MIMO smartphone," *IEEE Trans. Antennas Propag.*, vol. 68, no. 5, pp. 3487–3495, May 2020.

[17] L. Chang, Y. Yu, K. Wei, and H. Wang, "Polarization-orthogonal co-frequency dual antenna pair suitable for 5G MIMO smartphone with metallic bezels," *IEEE Trans. Antennas Propag.*, vol. 67, no. 8, pp. 5212–5220, Aug. 2019.

[18] A. Ren, Y. Liu, and C.-Y.-D. Sim, "A compact building block with two shared-aperture antennas for eight-antenna MIMO array in metal-rimmed smartphone," *IEEE Trans. Antennas Propag.*, vol. 67, no. 10, pp. 6430–6438, Oct. 2019.

[19] L. Sun, Y. Li, Z. Zhang, and Z. Feng, "Wideband 5G MIMO antenna with integrated orthogonal-mode dual-antenna pairs for metal-rimmed smartphones," *IEEE Trans. Antennas Propag.*, vol. 68, no. 4, pp. 3494–3503, Apr. 2020.

[20] L. Sun, Y. Li, Z. Zhang, and H. Wang, "Self-decoupled MIMO antenna pair with shared radiator for 5G smartphones," *IEEE Trans. Antennas Propag.*, vol. 68, no. 5, pp. 3423–3432, May 2020.

[21] A. A. Al-Hadi, J. Ilvonen, R. Valkonen, and V. Viikari, "Eight-element antenna array for diversity and MIMO mobile terminal in LTE 3500 MHz band," *Microw. Opt. Technol. Lett.*, vol. 56, no. 6, pp. 1323–1327, Jun. 2014.

[22] M.-Y. Li *et al.*, "Eight-port orthogonally dual-polarized antenna array for 5G smartphone applications," *IEEE Trans. Antennas Propag.*, vol. 64, no. 9, pp. 3820–3830, Sep. 2016.

[23] H. Xu, H. Zhou, S. Gao, H. Wang, and Y. Cheng, "Multimode decoupling technique with independent tuning characteristic for mobile terminals," *IEEE Trans. Antennas Propag.*, vol. 65, no. 12, pp. 6739–6751, Dec. 2017.

[24] J. Guo, L. Cui, C. Li, and B. Sun, "Side-edge frame printed eight-port dual-band antenna array for 5G smartphone applications," *IEEE Trans. Antennas Propag.*, vol. 66, no. 12, pp. 7412–7417, Dec. 2018.

[25] J.-Y. Deng, J. Yao, D.-Q. Sun, and L.-X. Guo, "Ten-element MIMO antenna for 5G terminals," *Microw. Opt. Technol. Lett.*, vol. 60, no. 12, pp. 3045–3049, Dec. 2018.

[26] D. Q. Liu, M. Zhang, H. J. Luo, H. L. Wen, and J. Wang, "Dual-band platform-free PIFA for 5G MIMO application of mobile devices," *IEEE Trans. Antennas Propag.*, vol. 66, no. 11, pp. 6328–6333, Nov. 2018.

[27] Q. Chen *et al.*, "Single ring slot-based antennas for metal-rimmed 4G/5G smartphones," *IEEE Trans. Antennas Propag.*, vol. 67, no. 3, pp. 1476–1487, Mar. 2019.

[28] D. Huang, Z. Du, and Y. Wang, "Slot antenna array for fifth generation metal frame mobile phone applications," *Int. J. RF Microw. Comput.-Aided Eng.*, vol. 29, no. 9, Sep. 2019, Art. no. e21841.

[29] W. Jiang, B. Liu, Y. Cui, and W. Hu, "High-isolation eight-element MIMO array for 5G smartphone applications," *IEEE Access*, vol. 7, pp. 34104–34112, 2019.

[30] Y. Li, C.-Y.-D. Sim, Y. Luo, and G. Yang, "12-port 5G massive MIMO antenna array in sub-6GHz mobile handset for LTE bands 42/43/46 applications," *IEEE Access*, vol. 6, pp. 344–354, 2018.

[31] Y. Li, C.-Y.-D. Sim, Y. Luo, and G. Yang, "High-isolation 3.5 GHz eight-antenna MIMO array using balanced open-slot antenna element for 5G smartphones," *IEEE Trans. Antennas Propag.*, vol. 67, no. 6, pp. 3820–3830, Jun. 2019.

[32] X. Zhang, Y. Li, W. Wang, and W. Shen, "Ultra-wideband 8-Port MIMO antenna array for 5G metal-frame smartphones," *IEEE Access*, vol. 7, pp. 72273–72282, 2019.

[33] Q. Cai, Y. Li, X. Zhang, and W. Shen, "Wideband MIMO antenna array covering 3.3–7.1 GHz for 5G metal-rimmed smartphone applications," *IEEE Access*, vol. 7, pp. 142070–142084, 2019.

[34] A. Zhao and Z. Ren, "Size reduction of self-isolated MIMO antenna system for 5G mobile phone applications," *IEEE Antennas Wireless Propag. Lett.*, vol. 18, no. 1, pp. 152–156, Jan. 2019.

[35] A. Zhao and Z. Ren, "Wideband MIMO antenna systems based on coupled-loop antenna for 5G N77/N78/N79 applications in mobile terminals," *IEEE Access*, vol. 7, pp. 93761–93771, 2019.

[36] A. Diallo, C. Luxey, P. Le Thuc, R. Staraj, and G. Kossiavas, "Study and reduction of the mutual coupling between two mobile phone PIFAs operating in the DCS1800 and UMTS bands," *IEEE Trans. Antennas Propag.*, vol. 54, no. 11, pp. 3063–3074, Nov. 2006.

[37] R. G. Vaughan and J. B. Andersen, "Antenna diversity in mobile communications," *IEEE Trans. Veh. Technol.*, vol. VT-36, no. 4, pp. 147–172, Nov. 1987.